

Theoretical investigation of a novel xylene-based light-driven unidirectional molecular motor

Cite as: J. Chem. Phys. 154, 064111 (2021); doi: 10.1063/5.0038281

Submitted: 23 November 2020 • Accepted: 20 January 2021 •

Published Online: 12 February 2021



F. Romeo-Gella,¹ I. Corral,^{1,a)} and S. Faraji^{2,a)}

AFFILIATIONS

¹Departamento de Química (Módulo 13, Facultad de Ciencias) and Institute of Advanced Chemical Sciences (IadChem), Universidad Autónoma de Madrid, Campus de Excelencia UAM-CSIC, Cantoblanco, 28049 Madrid, Spain

²Theoretical Chemistry Group, Zernike Institute for Advanced Materials, University of Groningen, Groningen, The Netherlands

Note: This paper is part of the JCP Special Collection in Honor of Women in Chemical Physics and Physical Chemistry.

a) Authors to whom correspondence should be addressed: ines.corral@uam.es and s.s.faraji@rug.nl

ABSTRACT

In this study, the working mechanism of the first light-driven rotary molecular motors used to control an eight-base-pair DNA hairpin has been investigated. In particular, this linker was reported to have promising photophysical properties under physiological conditions, which motivated our work at the quantum mechanical level. *Cis-trans* isomerization is triggered by photon absorption at wavelengths ranging 300 nm–400 nm, promoting the rotor to the first excited state, and it is mediated by an energy-accessible conical intersection from which the ground state is reached back. The interconversion between the resulting unstable isomer and its stable form occurs at physiological conditions in the ground state and is thermally activated. Here, we compare three theoretical frameworks, generally used in the quantum description of medium-size chemical systems: Linear-Response Time-Dependent Density Functional Theory (LR-TDDFT), Spin-Flip TDDFT (SF-TDDFT), and multistate complete active space second-order perturbation theory on state-averaged complete active space self consistent field wavefunctions (MS-CASPT2//SA-CASSCF). In particular, we show the importance of resorting to a multireference approach to study the rotational cycle of light-driven molecular motors due to the occurrence of geometries described by several configurations. We also assess the accuracy and computational cost of the SF-TDDFT method when compared to MS-CASPT2 and LR-TDDFT.

Published under license by AIP Publishing. <https://doi.org/10.1063/5.0038281>

I. INTRODUCTION

Exerting control over biological processes is a great challenge, which, if achieved, could revolutionize the fields of nanotechnology, biotechnology, and medicine.^{1–3} Biological processes occurring in cells are in fact very precisely controlled both in time and space in a natural manner, for instance, the widespread cellular signaling pathways in response to different agents.⁴ Externally achieving the control of the activity of biomolecules in these environments within the same spatial and temporal scales of nature could not only shed light into the course of these complex biochemical mechanisms but, at the same time, contribute to understanding the potential dysfunctions of these processes that eventually might trigger diseases. Light is perhaps one of the most convenient external agents for controlling these processes, as on the one hand, it is nowadays possible to fully adjust its wavelength, intensity, location, and timing, and on the other hand, it represents a non-invasive technique to living

tissues and avoids the contamination of biological samples.⁵ Following this spirit, molecular photoswitches, or light responsive molecules, capable of switching between at least two thermodynamically stable isomeric forms, have been used to control the structure of bioactive peptides, proteins, and nucleic acids' structure and function.⁶ Some of the most popular and promising photoswitches used for biotechnological purposes are azobenzene derivatives.^{7,8} This family undergoes reversible *cis-trans* isomerization, with high quantum yields, upon irradiation with non-destructive UV and visible wavelengths for biomolecules.⁹ A new twist in the field of photoregulation of biomolecules was proposed by Feringa and co-workers some years ago.^{10,11} They suggested the replacement of standard bi-stable photoswitches by overcrowded alkene-based rotary molecular motors (RMMs), whose rotary cycle is characterized by a multi-step process and four different isomers. Figure 1 shows a scheme of their rotary cycle, consisting of two light-driven steps followed, respectively, by two thermally activated steps, leading to an

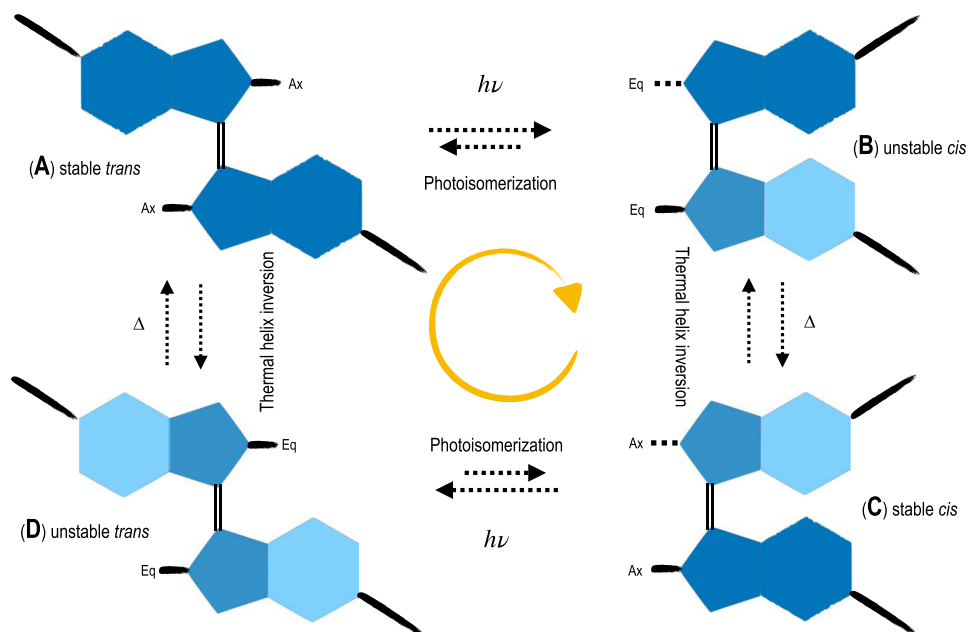


FIG. 1. Schematic representation of the four-step light-driven rotary molecular rotor¹² with its four metastable isomeric forms. Ax and Eq stand for axial and equatorial methyl groups, and the longer sticks represent the 3-hydroxypropyl substituents.

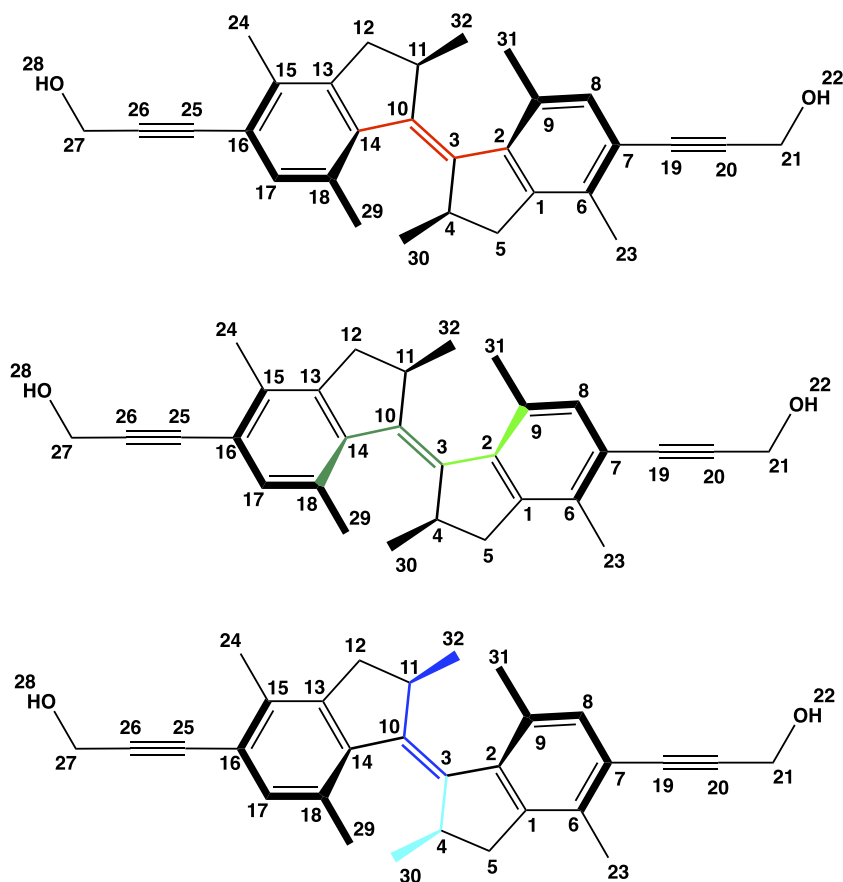


FIG. 2. Schematic representation with numbering of the heavy atoms (C and O) of the stable-*trans* isomer of RMM1 with coloring indicating the dihedrals taken into account as reaction coordinates: (top) α in red, (middle) β in light green and β' in dark green, and (bottom) γ in light blue and γ' in dark blue.

overall unidirectional rotation. The complete structure of the photoswitch is provided in Fig. 2. In particular, Lubbe *et al.* proposed a symmetric xylene-based rotor (RMM1),¹² consisting of four isomeric forms: stable- (A) and unstable-*trans* (D), and stable- (C) and unstable-*cis* (B).

During the light-driven steps, rotation along the C=C double bond [either from stable-*trans* (A) to unstable-*cis* (B) or from stable-*cis* (C) to unstable-*trans* (D)] takes place, but also an inversion of the helicity of the rotor subunits and the change of the relative orientation of the stereogenic methyl groups from axial to equatorial has been reported.¹² The photomediated steps are followed by thermally activated steps, in which the methyl groups come back to their original axial orientation and the helicity of the molecule is reverted, while the configuration of the double bond is maintained. Interestingly, photoswitch absorption occurs at wavelengths longer than 300 nm, preventing the simultaneous excitation of the DNA strand and, thus, its potential damage. The thermal helix inversion (THI) step, however, was reported to occur at temperatures slightly higher than the physiological one (67 °C), but reverse isomerization seems unlikely under those conditions. Altogether, the authors report a higher degree of photoregulation and structural change than other photoswitches, in a ratcheting-like fashion, which opens the field to further innovative applications. Finally, this RMM1 was introduced in a 16-mer of self-complementary A and T nucleobases, 8T-8A, leading to the new photoresponsive DNA hairpin 8T-RMM1-8A.¹² This system was reported to be the first molecular motor used to control successfully the secondary structure of DNA under physiological conditions.¹²

According to these experimental findings, we predict a ground state potential energy surface (PES) consisting of two pairs of minima in their stable and unstable conformations. A to B and C to D isomerization steps, i.e., light-activated reactions, are expected to be separated by high ground state energy barriers, while thermally driven steps (B to C and D to A) are characterized by lower energy barriers, surmountable at physiological conditions. However, accessible internal conversion seams between the excited and the ground states would assure fast and feasible photoisomerization. Despite the novelty and potential implication of these results, these experiments, which produce complicated spectra containing valuable information about the underlying processes, are difficult to interpret. Beyond any doubt, computer simulations, both static and time-resolved, can help us to unravel the photoswitching mechanism of the xylene intercalated hairpin at an atomic-level, providing detailed insight into the primary photo- and thermo-chemical reactions and to design a next generation of biohybrid systems capable of surpassing the performance of those that already exist. Here, we use advanced electronic structure methods to investigate the RMM1 photophysics and to provide detailed insight into its four-step rotatory cycle and the underlying driving force of the working mechanism and of the electronic structure evolution of the photoswitch. Additionally, we assess the performance of different quantum mechanical methods in the prediction and interpretation of the absorption spectra and in the description of the operating mechanisms, including the characterization of the various minima and internal conversion funnels.

This paper is organized as follows: Sec. II describes the computational details. Our results and discussion are presented in Sec. III, and finally, our concluding remarks are given in Sec. IV.

II. COMPUTATIONAL METHODS

Theoretical calculations have been performed in the frame of both Density Functional Theory (DFT) and wave function multireference methods. In particular, for the modeling of the photoisomerization mechanism, we have resorted to the popular multistate complete-active-space second-order perturbation theory (MS-CASPT2)¹³ method, employing complete-active-space self-consistent field (CASSCF) wave functions^{14–16} as a reference to capture both the static and dynamic fractions of the electronic correlation of these processes. Linear-Response Time-Dependent DFT (LR-TDDFT), despite describing dynamical electronic correlation, is based on a single reference framework, which prevents the proper description of non-adiabatic processes, such as internal conversion via conical intersections.^{17,18} An extension to TDDFT, called the Spin-Flip TDDFT (SF-TDDFT) method,¹⁸ in which a higher-spin triplet state is chosen as the initial reference allowing the ground state (S_0) and the singlet excited states to be treated on the same footing, was developed to describe strong nondynamical correlation and multiconfigurational events.^{18–23} This approach has shown a great performance for describing minimum energy crossing points (MECPs) in various systems,^{18,22–27} including stilbene, a prototype of photoswitch.²⁴

Ground state geometry optimizations ($S_{0,min}$) for both stable isomers (stable-*cis* and stable-*trans*) were performed at SF-B5050LYP/cc-pVDZ,^{18,28} both in the gas phase and in a continuum of dichloromethane, according to the Conductor-like Polarizable Continuum Model (C-PCM) scheme.^{29,30} Subsequent frequency calculations were undertaken at B5050LYP/cc-pVDZ to confirm the nature of the obtained minima, as spin-flip lacks analytical second derivative calculations, as implemented in Q-Chem 5.2.³¹ Relaxed potential energy surface (PES) scans for the S_0 were performed at the SF-B5050LYP/cc-pVDZ level of theory and along the following dihedrals (see Fig. 2): C₂–C₃–C₁₀–C₁₄ (α , red), C₉–C₂–C₃–C₁₀ (β , light green), C₁₈–C₁₄–C₁₀–C₃ (β' , dark green), C₁₀–C₃–C₄–C₃₀ (γ , light blue), and C₃–C₁₀–C₁₁–C₃₂ (γ' , dark blue). The α dihedral defines the actual isomerization reaction coordinate (*cis*–*trans*), β and β' describe the helix inversion, and γ and γ' refer to the relative stereogenic group orientation in each symmetric subunit (see C₃₀ and C₃₂ in Fig. 2). The geometries of all identified minima and transition states (TSs) were individually optimized, leading to the characterization of unstable-*cis*, unstable-*trans*, and transition states connecting each pair of isomers.

The vertical excitation energies (VEEs) of the first excited state, S_1 , were calculated for all $S_{0,min}$ geometries at different levels of theory for benchmarking purposes, namely, (a) LR-TDDFT with BLYP,^{36,37} B3LYP,³² B5050LYP, CAM-B3LYP,³³ and ω B97X-D³⁴ exchange-correlation functionals; (b) SF-TDDFT at the B5050LYP/cc-pVDZ level of theory; and (c) MS2-CASPT2(2,2)/ANO-S-VDZ^{13,35} and MS7-CASPT2(14,14)/ANO-S-VDZ, both with null IPEA shift³⁶ and 0.1 imaginary shift,³⁷ and using the Cholesky decomposition for approximating two electron integrals, within a convergence threshold of 10^{-6} a.u.³⁸ The active spaces used for the CASSCF wave functions were (2,2) containing HOMO and LUMO and (14,14) including all the π orbitals indicated in Fig. 3. In order to account for the solvent effects and also mimicking the experimental conditions,¹² LR-TDDFT and SF-TDDFT calculations were performed both in the gas phase and in a continuum of dichloromethane, as described by a C-PCM scheme.

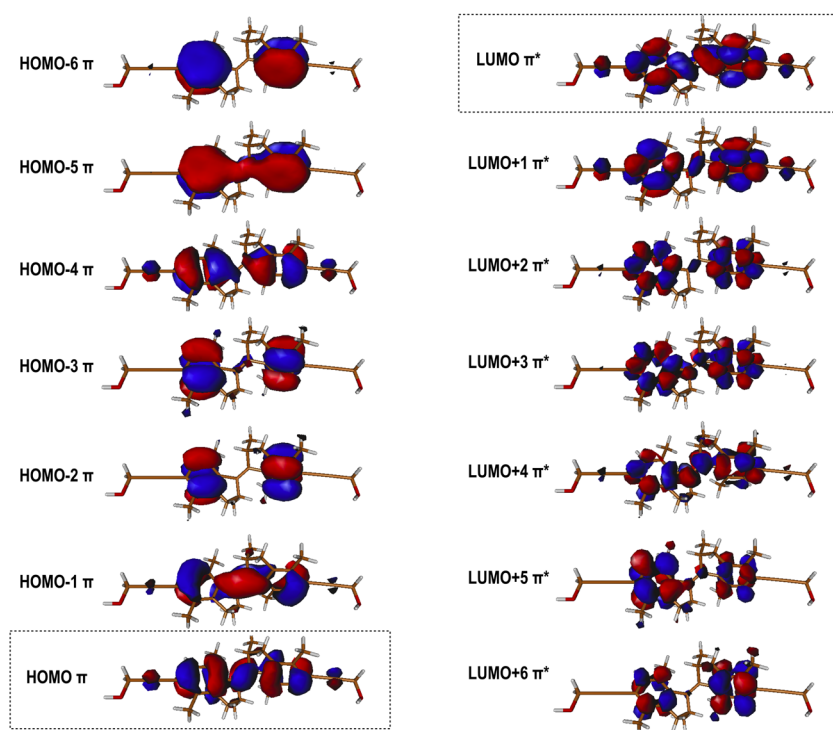


FIG. 3. SA7-CASSCF(14,14)/ANO-S-VDZ molecular orbitals included in the active space for the stable-*trans* isomer. Highlighted within a square the π_{HOMO} and π_{LUMO}^* orbitals involved in the first excited-state transition (S_1).

Excited-state ($S_{1,min}$) geometries were calculated at the LR-B5050LYP/cc-pVDZ, SF-B5050LYP/cc-pVDZ, and SA2-CASSCF(2,2)/ANO-S-VDZ levels of theory. Additionally, relaxed PES scans of the S_1 were done at the SF-B5050LYP/cc-pVDZ level of theory along the α dihedral. The minimum energy crossing points (MECPs) between S_1/S_0 were located at the SF-B5050LYP/cc-pVDZ level, using the penalty function³⁹ algorithm, and at the SA2-CASSCF(2,2)/ANO-S-VDZ level, using the gradient projection method.⁴⁰

All DFT-based calculations have been performed with the Q-Chem 5.2³¹ electronic structure program. OpenMolcas⁴¹ was used for all wave function-based calculations, and the corresponding MECP/CI optimizations at the SA-CASSCF(2,2) level of theory were performed using BAGEL.⁴²

III. RESULTS AND DISCUSSION

A. Ground-state stationary geometries

Stable-*cis* (C) and stable-*trans* (A) optimized $S_{0,min}$ geometries have been obtained at different levels of theory, assessing also the solvent effect on their structures. In particular, LR- ω B97X-D/cc-pVDZ, LR-B5050LYP/cc-pVDZ, and SF-B5050LYP/cc-pVDZ optimized geometries, both in the gas phase and including the solvent (dichloromethane) adopting a C-PCM scheme, were compared. Tables I and II show the values of the main reaction coordinates (dihedrals defined in Sec. II) along the rotary cycle for each of the optimized geometries. No significant deviation of any dihedral in any environment condition or level of theory is observed. These findings lead us to conclude that (a) the inclusion of dispersion, as

in ω B97X-D, (b) the effect of using a triplet reference for the $S_{0,min}$ optimization by the SF approach, (c) the inclusion of 50% Hartree-Fock (HF) exchange, as in B5050LYP, and (d) the incorporation of dichloromethane as a solvent do not have any significant effect on the dihedrals, considered as reaction coordinates in this work, of the $S_{0,min}$ geometries of the RMM1.

The most important parameters of the $S_{0,min}$ optimized geometries and relative energies at SF-B5050LYP/cc-pVDZ are reported in Table II for the four isomers: A, B, C, and D. The lowest energy isomer, stable-*cis* (C), is set as the energy reference. The stable-*cis* (C) and the stable-*trans* (A) isomers, which energetically differ by 2.46 Kcal/mol, are the most stable structures, when compared to their unstable form, in agreement with the experimental findings.¹² We have also successfully located the unstable-*cis* (B) and unstable-*trans* (D) isomers with higher energies. In accordance with a Boltzmann distribution, under physiological conditions, the population of C and A isomers against B and D would be of 100% and 96%, in agreement with the relative population of the ground state species experimentally reported.¹² As given in Table II, while photoisomerization (A to B and C to D) is mainly determined by a 180° α rotation, thermal helix inversion from unstable to stable isomers (B to C and D to A) occurs along β and γ coordinates, with moderate changes in the α value. This involves the inversion of dihedral β from negative to positive values, indicating the relative helicity inversion of the two subunits, and the change of the stereogenic methyl groups from equatorial to axial conformation, as indicated by more negative values of dihedral γ .

The thermally activated steps, connecting each unstable to its respective stable isomer, are mediated by a ground-state transition state (TS), as reported in Table II. We found an energy

TABLE I. Dihedral values (in degrees) for the $S_{0,min}$ optimized geometries of stable-*cis* and stable-*trans* isomers obtained at different levels of theory in the gas phase and dichloromethane (DCM).

Species	Level of theory	Environment	α	β	β'	γ	γ'
Stable- <i>trans</i> (A)	LR- ω B97X-D	Gas phase	160.5	49.1	48.7	−119.1	−118.8
	LR- ω B97X-D	DCM	160.4	48.8	48.7	−118.7	−118.7
	LR-B5050LYP	Gas phase	160.9	48.5	48.7	−118.1	−118.2
	LR-B5050LYP	DCM	160.8	48.3	48.6	−117.8	−118.1
	SF-B5050LYP	Gas phase	161.1	48.1	48.5	−117.9	−118.2
	SF-B5050LYP	DCM	161.0	48.1	48.4	−117.7	−117.9
Stable- <i>cis</i> (C)	LR- ω B97X-D	Gas phase	6.2	37.4	37.5	−100.0	−99.7
	LR- ω B97X-D	DCM	6.4	37.4	37.4	−99.6	−99.4
	LR-B5050LYP	Gas phase	6.4	37.1	37.3	−99.1	−99.1
	LR-B5050LYP	DCM	6.6	37.0	37.1	−98.8	−98.7
	SF-B5050LYP	Gas phase	5.8	37.5	37.6	−99.4	−99.4
	SF-B5050LYP	DCM	6.1	37.2	37.3	−98.9	−98.9

barrier of 19.1 Kcal/mol for the *trans* (TS_{DA}) pair and 25.3 Kcal/mol for the *cis* (TS_{BC}) pair, which is in agreement with the available experimental data, 24.8 Kcal/mol.¹² It must be noted that experimentally unstable-*trans* (D) is reported to have a much shorter lifetime compared to unstable-*cis* (B), which is also consistent with the calculated difference in the energy barriers according to a simple kinetic model calculation. Still, small differences between the experimental and our theoretical results might arise due to the fact that our calculations employ potential energies instead of Gibbs free energies. Additionally, the scan of the ground state potential energy surface along the *cis-trans* isomerization coordinate (α) revealed high energy barriers connecting isomers A–B and C–D. Nevertheless, the multireference character of the TS guesses did not enable their characterization at this level; thus, TS_{AB} and TS_{CD} refer in Table II to the maxima of the relaxed potential energy scan along the α dihedral at the SF-B5050LYP level of theory and not the actual TS optimized geometries. Regardless of this issue, we predict energy barriers of ~ 50 Kcal/mol, which would prevent thermal *cis-trans* isomerization reactions to occur.

B. Vertical excitation energies

The S_1 vertical excitation energies (VEEs) for the stable-*trans* and unstable-*cis* isomers obtained at LR-TDDFT (various functionals) and SF-TDDFT levels of theory as well as experimental¹² and

additional theoretical results using wave function based methods are summarized in Table III. One observes the typical blueshift of the S_1 VEE to higher excitation energies when the fraction of Hartree–Fock (HF) exchange is increased from zero (BLYP) to 20% (B3LYP) and finally to 50% (B5050LYP). The state order remains the same for the functionals with HF fractions greater than zero, and it is similar to the state order for SF-TDDFT and MS-CASPT2 with all the methods considered, showing S_1 to be the bright state. The molecular orbitals ($\pi_{HOMO}\pi_{LUMO}^*$) involved in this excitation, although considerably delocalized throughout the π system of the molecule, are mainly localized in the central C=C bond [see Fig. 3]. The rest of the low-lying states described in our calculations have also a $\pi\pi^*$ character with rare participation of the lone pairs of the oxygen atoms located in the extremes of the molecule. In particular, the main character of the lowest lying excited states S_2 , S_3 , and S_4 is $\pi_{HOMO-3}\pi_{LUMO}^*$, $\pi_{HOMO-2}\pi_{LUMO}^*$, and $\pi_{HOMO}\pi_{LUMO+1}^*$, respectively, according to LR-B5050LYP and MS7-CASPT2(14,14). This suggests that our rotary molecular motor can be satisfactorily described by TDDFT because of its closed-shell configuration, being also a planar molecule not prone to intramolecular charge transfer. In addition, increasing the size of the basis set by adding diffuse basis functions has a negligible effect on the excitation energy and state order, suggesting the local character of the excited states.⁴³

TABLE II. Energy (in Kcal/mol) and dihedral values (in degrees) for the relevant stationary points of the ground state potential energy surface at the spin-flip B5050LYP/cc-pVDZ level of theory in the gas phase.

Species	Energy (Kcal/mol)	α	β	β'	γ	γ'
Unstable- <i>trans</i> (D)	5.54	162.0	−36.2	−35.9	−22.6	−22.8
TS_{trans} (TS_{DA})	24.59	173.6	2.9	3.8	−76.4	−76.4
Stable- <i>trans</i> (A)	2.46	161.1	48.1	48.5	−117.9	−118.2
Unstable- <i>cis</i> (B)	4.27	−26.7	−28.7	−28.6	−31.6	−32.0
TS_{cis} (TS_{BC})	29.61	1.1	67.7	−70.6	−129.1	21.0
Stable- <i>cis</i> (C)	0.00	5.8	37.5	37.6	−99.4	−99.4

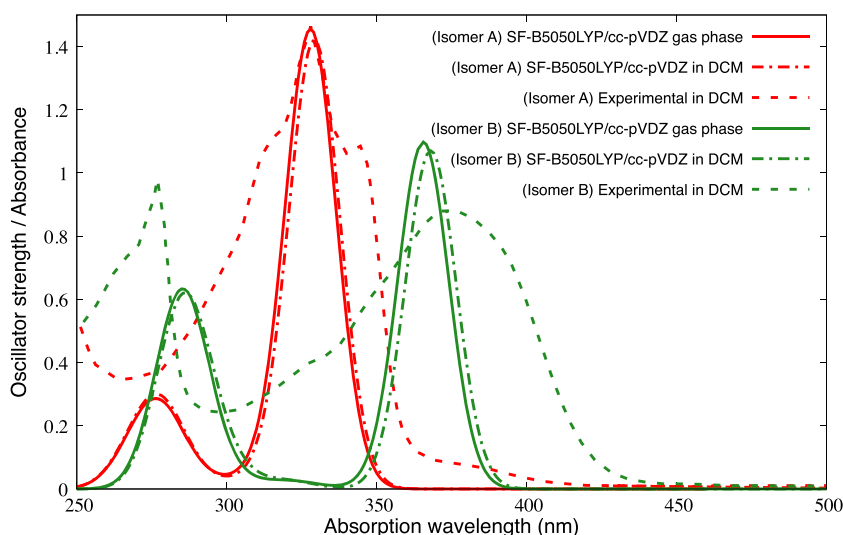
TABLE III. S_1 vertical excitation energies in the gas phase and in dichloromethane (DCM) and solvent shift (ΔE) of the stable-*trans* (A) and unstable-*cis* (B) calculated at different levels of theory.

Excitation energy, eV/nm (osc. strength)			ΔE (eV)	Excitation energy, eV/nm (osc. strength)		ΔE (eV)
Environment	Gas phase	DCM		Gas phase	DCM	
Isomer	Stable- <i>trans</i> (A)			Unstable- <i>cis</i> (B)		
LR-BLYP	3.29/377(1.0)	3.22/385(1.3)	−0.07	3.04/408(1.0)	2.91/426(1.2)	−0.13
LR-B3LYP	3.78/328(1.4)	3.68/337(1.6)	−0.10	3.37/368(1.1)	3.23/384(1.3)	−0.14
LR-B5050LYP	4.27/290(1.6)	4.18/297(1.8)	−0.09	3.73/332(1.2)	3.60/344(1.3)	−0.13
LR-CAM-B3LYP	4.26/291(1.6)	4.16/298(1.8)	−0.10	3.71/334(1.2)	3.59/345(1.3)	−0.12
LR- ω B97X-D	4.30/288(1.6)	4.20/295(1.8)	−0.10	3.74/332(1.1)	3.62/343(1.3)	−0.12
SF-B5050LYP	4.46/278(1.5)	4.44/279(1.4)	−0.02	3.84/323(1.1)	3.80/326(1.1)	−0.04
MS2-CASPT2(2,2)	3.95/314(1.04)	3.38/367(0.8)
MS7-CASPT2(14,14)	3.68/337(0.8)	3.28/378(0.6)
Experiment ¹²	3.74 (328)			3.32 (373)		

A closer inspection reveals that B5050LYP with 50% HF exchange gives similar results to long-range corrected (LC) functionals, such as ω B97X-D³⁴ or CAM-B3LYP,³³ which have been designed to overcome limitations associated with the traditional exchange-correlation functionals, e.g., overestimating π bond breaking and proper description of charge-transfer phenomena.^{44–50} Comparing the performance of LR-TDDFT calculations, in Table III, it is apparent that functionals containing larger amount of HF exchange ($\geq 50\%$), i.e., B5050LYP, ω B97X-D, and CAM-B3LYP, deliver similar excitation energies and also close enough to experimental values,¹² despite not being the most accurate ones. Nevertheless, for this particular system, as discussed in Sec. III A, due to the occurrence of conical intersections and relevant geometries with considerable multireference character, it is safer to use SF-TDDFT

to properly describe the electronic configuration of the molecule, in particular, in the S_1 state. In addition, earlier studies^{19–21,23,26} have revealed that BHHLYP, and also B5050LYP due to their resemblance, are suitable functionals when describing excited states and MECF optimizations within SF-TDDFT methodology.

In order to shed further light on the effect of the solvent on the absorption spectra, the VEEs at the LR- and SF-TDDFT levels of theory are calculated within the C-PCM scheme. The corresponding bathochromic shifts are also reported in Table III. In the case of LC and B5050LYP functionals, inclusion of the solvent effect shifts the theoretical values slightly closer to experimental ones. This effect is also depicted in Fig. 4 at the SF-TDDFT level of theory, where computed gas-phase and solvent VEEs are compared to experimental UV-Vis absorption spectra.¹² The bathochromic shift for SF-TDDFT is

**FIG. 4.** Experimental and calculated absorption spectra (FWHM = 10 nm) of the stable-*trans* (A; red) and unstable-*cis* (B; green) at the SF-B5050LYP/cc-pVDZ level of theory in the gas phase and in DCM. Experimental absorption spectra were re-plotted with the data provided in Ref. 12. The calculated spectra have been shifted 50 nm (0.59 eV) to longer wavelengths to fit the experimental peaks.

considerably smaller than those reported by LR-TDDFT, but still the trend is comparable.

For the sake of completeness, SF-TDDFT and LR-TDDFT VEEs were compared to the absorptions computed with MS-CASPT2 and SA-CASSCF methods in the gas phase.^{25,51} The impact of the number of roots and the size of the active space in the VEEs was extensively explored. A reasonable active space balancing accuracy and computational cost was set to the (14,14) scheme including 7 π and 7 π^* orbitals [see Fig. 3]. Oxygen lone pairs, as reported above, were not found to participate in low-lying excitations, so they were excluded from the active space. Thus, S_1 VEEs were calculated in the gas phase at the MS7-CASPT2(14,14)/ANO-S-VDZ and MS2-CASPT2(2,2)/ANO-S-VDZ levels of theory. A closer agreement with experimental values has been obtained upon increasing the size of the active space (see Table III and Table S1).

Our MS7-CASPT2(14,14) gas phase calculation shows a bright S_0 – S_1 electronic transition at 337 nm for the stable-*trans* (A) isomer, which is close to the experimentally reported absorption peak at 328 nm.¹² For unstable-*cis* (B), MS7-CASPT2(14,14) predicts S_1 absorption at 378 nm, which matches well with the experimental values. Table S1 shows a comparison of the S_1 excitation energies for the four $S_{0,min}$ geometries obtained at different levels of theory. It must be noted that the experimental values are reported in solution, while our MS7-CASPT2 results are calculated in the gas phase. From these results, we conclude that the SF-TDDFT overestimates the VEEs in line with previously reported trends for several organic compounds.⁵² A similar trend, although smoother, is observed for the LR-TDDFT VEE values. It is important to note that all the levels of theory were able to reproduce the experimentally observed shift between the absorptions of stable-*trans* (A) and unstable-*cis* (B) isomers. For instance, the first absorption shifts, from stable-*trans* (A) to unstable-*cis* (B), by 0.62 eV, 0.56 eV, and 0.40 eV according to SF-B5050LYP, LR- ω B97X-D, and MS7-CASPT2(14,14), respectively, matching considerably well with the experimental photochromic shift of 0.42 eV.¹²

C. Excited-state stationary geometries

The excited-state nonadiabatic dynamics of a chromophore is essentially controlled by the internal energy of the system after irradiation, the occurrence of minima along the excited PES, the electronic couplings, and the accessibility of non-radiative funnels for the transfer of population between states of the same or different multiplicity.^{53,54} While for the $S_{0,min}$ geometries, single reference electronic structure methods, such as DFT, usually provide sufficiently accurate results, the correct characterization of $S_{1,min}$ geometries and, in particular, of conical intersections and other MECPs might require more than one electronic configuration and therefore calls for multireference electronic structure methods. This is indeed the case for the system considered in this work, in which the relative rotation of both symmetric subunits (along the α coordinate) breaks the conjugation of the system, favored by the electronic transition from the HOMO (π) to the LUMO (π^*) (see Fig. 3). To assess the performance of the different methods used in this study, in the description of the excited states involved in the first steps of the photoisomerization, S_1 optimizations were performed at the LR-TDDFT, SF-TDDFT, and SA2-CASSCF(2,2), including HOMO and LUMO as a minimal active space, levels of theory. Table IV shows the geometric parameters for the four $S_{1,min}$ isomers at the different levels of theory. While SF-TDDFT and SA-CASSCF report similar $S_{1,min}$ geometries for all isomers, LR-TDDFT geometries differ significantly from those calculated by the other methods (in particular, considering the photoisomerization coordinate α), except for the stable-*trans* isomer. For this isomer, all levels of theory deliver similar geometries, which are not far from $S_{0,min}$, and thus are well described even by the single reference LR-TDDFT approach. Interestingly, the inclusion of static correlation in the wave function enhances further rotation along the α reaction coordinate, in particular, when approaching the conical intersection, as will be discussed later in this section.

Aiming at classifying, as low $M \leq 0.05$, moderate $0.05 \leq M \leq 0.1$, or strong $M \geq 0.1$, the multiconfigurational character of the

TABLE IV. Dihedral values (in degrees) for the $S_{1,min}$ optimized geometries obtained at different levels of theory in the gas phase and its respective M diagnostic values.

Species	Level of theory	α	β	β'	γ	γ'	M diagnostic
Stable- <i>trans</i> (A)	LR-B5050LYP	165.6	43.9	44.7	−116.8	−117.4	0.013 318
	SF-B5050LYP	164.9	42.1	45.5	−115.1	−117.0	...
	SA2-CASSCF(2,2)	167.7	43.5	44.9	−117.4	−118.1	0.014 058
Unstable- <i>trans</i> (D)	LR-B5050LYP	135.5	−20.8	−22.2	−28.3	−26.9	0.119 004
	SF-B5050LYP	74.9	21.3	−11.9	−63.1	−32.2	...
	SA2-CASSCF(2,2)	79.5	13.8	−10.3	−58.7	−35.5	0.047 415
Stable- <i>cis</i> (C)	LR-B5050LYP	47.2	18.4	18.4	−84.2	−84.4	0.059 469
	SF-B5050LYP	52.5	16.7	17.0	−84.9	−85.3	...
	SA2-CASSCF(2,2)	71.4	7.8	24.1	−74.6	−91.1	0.139 534
Unstable- <i>cis</i> (B)	LR-B5050LYP	−69.3	−3.5	−2.9	−47.9	−49.5	0.179 594
	SF-B5050LYP	−115.2	33.6	0.8	−71.2	−42.3	...
	SA2-CASSCF(2,2)	−111.1	28.4	3.1	−67.7	−46.1	0.124 133

TABLE V. Energy (in kcal/mol) and dihedral values (in degrees) for the relevant critical points of the S_1 potential energy surface at the spin-flip B5050LYP/cc-pVDZ level of theory in the gas phase.

Species	S_1 energy (eV)	α	β	β'	γ	γ'
Stable- <i>trans</i> (A) $S_{0,min}$	4.57	160.5	49.1	48.7	−119.1	−118.8
Stable- <i>trans</i> (A) $S_{1,min}$	4.07	164.9	42.1	45.5	−115.1	−117.0
CI $_{S_1/S_0}$	3.58	−131.8	−1.6	53.1	−38.2	−79.2
Unstable- <i>cis</i> (B) $S_{1,min}$	3.37	−115.2	33.6	0.8	−71.2	−42.3
Unstable- <i>cis</i> (B) $S_{0,min}$	4.24	−25.6	−29.6	−29.2	−30.6	−31.1
Stable- <i>cis</i> (C) $S_{0,min}$	4.24	6.2	37.4	37.5	−100.0	−99.8
Stable- <i>cis</i> (C) $S_{1,min}$	3.53	52.5	16.7	17.0	−84.9	−85.3
CI' $_{S_1/S_0}$	3.59	55.0	49.1	−17.7	−71.4	−23.3
Unstable- <i>trans</i> (D) $S_{1,min}$	3.27	74.9	21.3	−11.9	−63.1	−32.2
Unstable- <i>trans</i> (D) $S_{0,min}$	4.23	163.1	−37.0	−37.0	−21.5	−21.7

system along the photoreactive pathway, we used the well-known M diagnostic⁵⁵ by Truhlar and co-workers on the CASSCF(2,2) wave functions of the ground state at the minima of the S_1 PES. The M values are reported in Table IV. Our results indicate a medium to strong multireference character for the S_0 wave functions at these regions of the PES, which is in line with the failure of LR wave functions to obtain correct geometries in contrast to SF and CASSCF wave functions. Based on the results showed in this section and Secs. III A and III B, due to the widespread occurrence of wave functions described by several configurations along the whole isomerization space, in the following, we will restrict ourselves to SF-B5050LYP and CASSCF results.

Table V reports the energy and the geometric parameters of the stationary points in the S_1 PES at the SF-B5050LYP/cc-pVDZ level of theory. These results reveal the evolution of the coordinate α upon light absorption, but also the abrupt change in the coordinates β and γ , along the S_1 state.

Finally, also relevant to the scrutiny of photoisomerization mechanism of these rotors are the MECPs, which were obtained as described in Sec. II starting from each isomer geometry. Considering the limitations of LR-TDDFT for the description of PES regions with considerable multireference character, SF-TDDFT and SA-CASSCF were employed for the characterization of internal conversion funnels (see Table VI). Two different MECPs were found, CI $_{S_1/S_0}$ and CI' $_{S_1/S_0}$, connecting the isomer A with B, and C with D, respectively. Their optimized geometric parameters and relative energies are reported in Table VI at the SF-B5050LYP and SA2-CASSCF(2,2)

levels of theory. It is apparent that both the SF and the multireference methodologies return similar geometries for the MECPs, halfway of the light-activated steps, coinciding with the highest energy point when performing a constrained optimization along the α dihedral at S_0 . The energies of the two states involved in the MECP optimization, the norm of the derivative coupling, and the α dihedral values along the MECPs optimization trajectories are given in Figs. S1 and S2. Accessibility of these crossing seams is plausible, in terms of energy, considering that the reported CIs lie below the initial absorption energy (see Table V). This point will be commented in depth in Sec. III D. Additionally, since the results of both SF-B5050LYP and SA2-CASSCF(2,2) methodologies are equivalent, we will stick to the first one for further discussion.

CI $_{S_1/S_0}$ was obtained starting from stable-*trans* (A) and unstable-*cis* (B) geometries. Both optimizations converged to the same geometry, characterized by an α value of -132° , similar to that of unstable-*cis* (B) $S_{1,min}$, although the crossing takes place slightly higher in energy (0.21 eV). This indicates that this MECP is close to the unstable-*cis* (B) $S_{1,min}$ and that it is energetically accessible, in particular, taking into account the excess of vibrational energy after photon absorption from $S_{0,min}$. The norm of the non-adiabatic coupling was computed at each optimization step, and its value increased from starting values of <0.1 to >50 in the optimized MECPs, as reported in Fig. S1. Additional MECPs on this side of the rotary cycle were not found, and although the existence of additional internal conversion funnels cannot be ruled out, it seems plausible that CI $_{S_1/S_0}$ is the main non-adiabatic relaxation seam due to its proximity to the stable-*trans* (A) and unstable-*cis* (B) $S_{1,min}$ and thus its accessibility.

CI' $_{S_1/S_0}$ was obtained starting from the stable-*cis* (C) and unstable-*trans* (D) geometries. Again, the same geometry was obtained from both calculations, reporting an α dihedral value of 55° . This funnel lies 0.06 eV and 0.32 eV higher than the stable-*cis* (C) $S_{1,min}$ and the unstable-*trans* (D) $S_{1,min}$, respectively. After photoexcitation, the excess of vibrational energy will be enough to reach the CI' $_{S_1/S_0}$ geometry, from either $S_{1,min}$, returning the excited population back to the S_0 PES. The same behavior was observed for the norm of the non-adiabatic coupling, as can be seen in Fig. S2. Again, no extra S_1/S_0 MECPs were found for this part of the rotary cycle,

TABLE VI. Dihedral values (in degrees) for the S_1/S_0 MECPs obtained from the A and B isomers' geometries at different levels of theory in the gas phase.

Species	Level of theory	α	β	β'	γ	γ'
CI $_{S_1/S_0}$	SF-B5050LYP	−131.8	−1.6	53.1	−38.2	−79.2
	SA2-CASSCF(2,2)	−132.2	−1.6	55.7	−38.2	−81.2
CI' $_{S_1/S_0}$	SF-B5050LYP	55.0	49.1	−17.7	−71.4	−23.3
	SA2-CASSCF(2,2)	51.0	54.0	−17.9	−73.1	−24.5

which supports the idea that CI'_{S_1/S_0} is the main internal conversion funnel back to the ground state, due to its energetic accessibility and its geometric proximity to $S_{1,min}$.

D. Potential energy surface

In this section, we highlight and summarize the main features on the PES responsible for the rotation mechanism of this molecule upon light absorption. Figure 5 shows the S_0 and S_1 PES along the main reaction coordinate (dihedral α) of the photoisomerization. Four minima have been characterized in the S_0 PES, corresponding to the metastable isomeric forms: stable-*trans*, unstable-*cis*, stable-*cis*, and unstable-*trans* (A, B, C, and D, respectively, in Figs. 1 and 5). Furthermore, two transition states were characterized along the β and γ coordinates mediating thermally driven helix inversion between (i) unstable-*cis* and stable-*cis* (TS_{BC}) and (ii) unstable-*trans* and stable-*trans* (TS_{AD}). As discussed in Sec. III A, the energy barriers [19.1 kcal/mol (0.82 eV) and 25.3 Kcal/mol (1.10 eV) for the TS_{BC} and TS_{DA} , respectively] are low enough to be surpassed at physiological conditions in a reasonable amount of time, 6 h at 40 °C, as reported by the instrumentalists.¹² On the

other hand, energy barriers of ~50 kcal/mol were found for TS_{AB} and TS_{CD} along the α dihedral coordinate. These high barriers practically exclude the thermal isomerization and support the photoisomerization reaction as the operative pathway under physiological conditions.

Upon light absorption, the ground state of stable-*trans* (A) isomer ($\alpha = 161^\circ$) is excited to the bright S_1 with an energy of 4.57 eV. From the Franck–Condon geometry, after vibrational relaxation, the $S_{1,min}$ (A) ($\alpha = 165^\circ$) is reached with an energy of about 4.07 eV. A small energy barrier of <2 kcal/mol separates this minimum from a downhill potential energy profile, leading to $S_{1,min}$ (B), along which it hits CI_{S_1/S_0} . This behavior is typical of processes with CIs accessible from the FC region without significant energy barriers, which is the case here. From the reversed side, the ground state unstable-*cis* (B) population ($\alpha = -26^\circ$) can be excited to S_1 at 4.24 eV and then relaxes downhill to its $S_{1,min}$ (B) ($\alpha = -115^\circ$) with an energy of 3.37 eV. The unstable-*cis* (B) $S_{1,min}$ geometry is close, both energetically and structurally, to the CI_{S_1/S_0} ($\alpha = -132^\circ$), from where the S_0 PES can be accessed through internal conversion. Once in the S_0 , the population can bifurcate to either the stable-*trans* $S_{0,min}$ (A) or the unstable-*cis* $S_{0,min}$ (B), the latter resulting in successful photoisomerization.

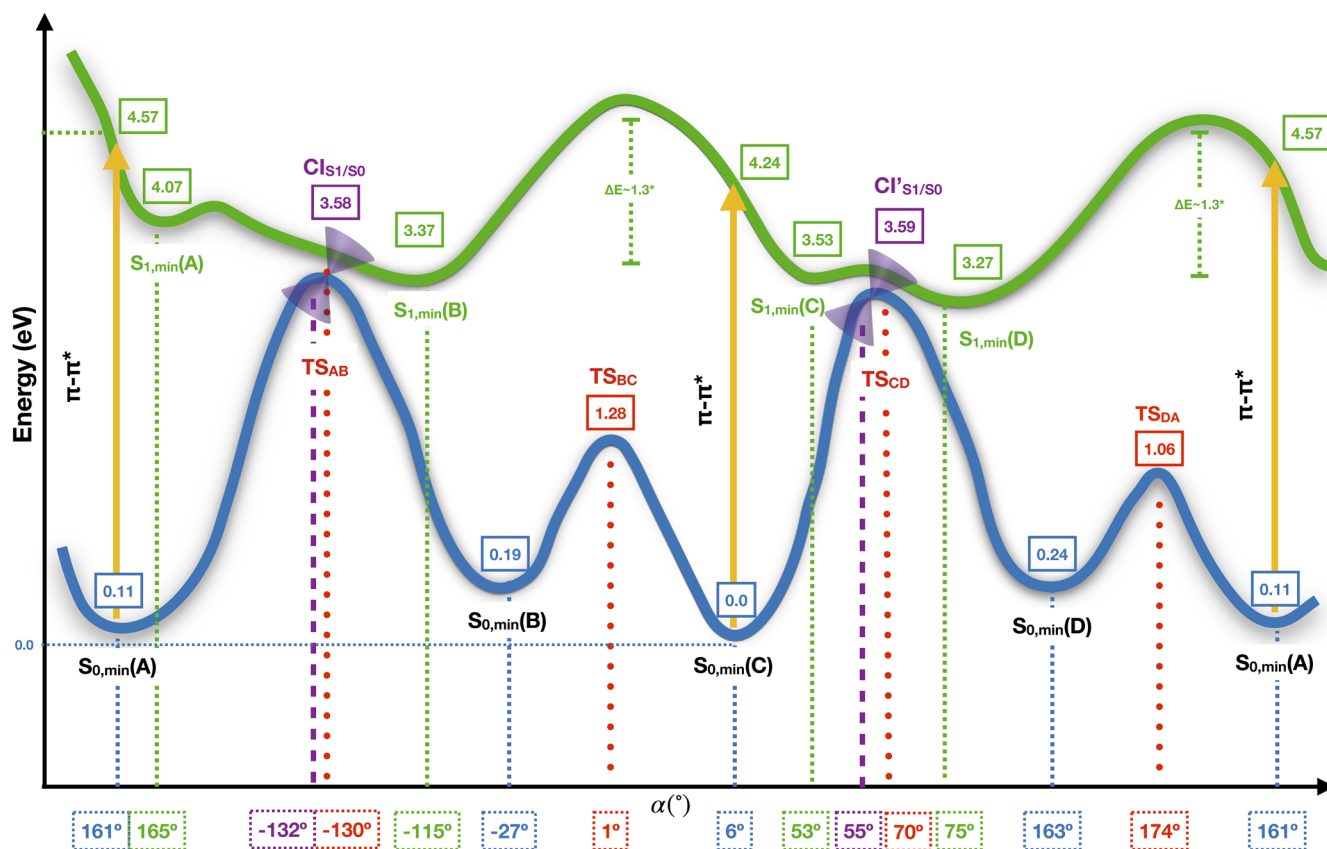


FIG. 5. PES scheme for the rotary cycle of the RMM. Energies computed at the spin-flip B5050LYP/cc-pVDZ level of theory and relative to the stable-*cis* ground state energy in eV. Color code: (blue) ground state, (green) first excited state, (purple) degeneracy regions, and (red) transition states. Letter code: (A) stable-*trans*, (B) unstable-*cis*, (C) stable-*cis*, and (D) unstable-*trans* isomers.

In a similar fashion, after photon absorption, the stable-*cis* $S_{0,min}(C)$ ($\alpha = 6^\circ$) is vertically excited to the first (bright) excited state with an energy of 4.24 eV, from where it undergoes vibrational relaxation until reaching $S_{1,min}(C)$ ($\alpha = 53^\circ$). From this point, only 0.6 eV higher in energy, CI'_{S_1/S_0} ($\alpha = 55^\circ$) can be reached. Analogously, the unstable-*trans* $S_{0,min}(D)$ ($\alpha = 163^\circ$) can be vertically excited with an energy of 4.23 eV, from where it undergoes a vibrational relaxation toward $S_{1,min}(D)$ ($\alpha = 75^\circ$) with an energy of 3.27 eV. From this point, CI'_{S_1/S_0} that acts again as a doorway for an internal conversion to the ground state is accessible (0.32 eV higher), considering the vibrational excess of energy. After internal conversion to the ground state, the system can evolve either to the stable-*cis* (C) or unstable-*trans* (D), the latter resulting in successful photoisomerization.

Altogether, the directionality of the photoisomerization is determined by the negative gradient, which brings the molecule close to the conical intersection, whose accessibility, in terms of energy and geometry, supports the non-adiabatic radiationless transition, leading the excited population back to the ground state. Furthermore, it is remarkable the ability of the system to access both CIs from each of the isomers involved in the transition, making possible the reversibility of the photoisomerization before thermal helix inversion takes place, as experimental data showed for the A–B pair of isomers.¹² In fact, according to our results, the same behavior should be registered for the C–D pair of isomers, although THI was reported to be fast in Ref. 12. Overall, the speed of the complete rotation seems to be constrained by the thermally activated helix inversion rate-determining step with an energy barrier relatively accessible at physiological conditions.

IV. CONCLUSION

Throughout this study, we carried out a series of quantum mechanical calculations to systematically study the four-step light-driven rotatory cycle of RMM1 reported by Lubbe *et al.*¹² (see Figs. 1 and 2). Additionally, we have assessed the validity of different theoretical approaches in the description of the different light-driven and thermally driven steps, unraveling the working mechanism at the molecular level of this system. Upon light absorption, the RMM1 molecule is electronically excited to its first (bright) excited state S_1 , from where it is able to isomerize from *trans* to *cis* and vice versa, via ultra-fast S_1 to S_0 internal conversion mediated by non-adiabatic couplings and accessible MECPs located in the vicinity of $S_{1,min}$ of the corresponding isomeric forms. Interestingly, our results indicate the possibility of photoreversion for each *cis*–*trans* isomerization, provided that the thermal-helix inversion has not taken place, which is in line with the experimental data.¹²

The estimation of the quantum yield of the photo-induced steps should be tackled using dynamical methods, and the work in this direction is in progress in our group. The required energy barrier for the thermally driven helicity inversion steps, along which an unstable isomer converts to its corresponding stable form, is estimated to be approximately 20–25 kcal/mol, which can still be surpassed, after some time, at physiological conditions. Our results suggest that the rate-determining steps are the two thermally driven helicity inversion steps; thus, future research should address the reduction of this energy barrier to further accelerate and increase the efficiency of the overall rotatory process.

Finally, the spin-flip TDDFT scheme has been reported as a cheaper alternative to the widespread multireference CASSCF-based methods, producing good reference geometries both in regions described by a single predominant configuration and in those where static electronic correlation is strong. Although SF-TDDFT was found to slightly overestimate absorption energies in comparison to MS-CASPT2 and LR-TDDFT methodologies, consistent results have been obtained with this approach. Overall, SF-TDDFT has been shown to produce more accurate and realistic $S_{1,min}$ and MECP geometries than the conventional LR-TDDFT method, which might produce inaccurate excited state PES critical points, when static correlation plays an important role. This study provides further evidence for the applicability of the SF-TDDFT for describing both excited and ground states and thus can be considered as a good low-cost method to study medium- to large-size systems of comparable complexity.

SUPPLEMENTARY MATERIAL

See the [supplementary material](#) for additional and supporting data. Table S1 summarizes the vertical excitation energies for the four isomers at different levels of theory. Figures S1 and S2 show a graphical representation of the convergence of the conical intersection search calculations for CI_{S_1/S_0} and CI'_{S_1/S_0} .

ACKNOWLEDGMENTS

The project that gave rise to these results received the support of a fellowship from “la Caixa” Foundation (Grant No. ID 100010434). The fellowship code is Grant No. LCF/BQ/DR19/11740024. Additionally, the work was performed under the Project HPC-EUROPA3 (INFRAIA-2016-1-730897) with the support of the EC Research Innovation Action under the H2020 Program; in particular, the authors gratefully acknowledge the computer resources and technical support provided by SURFSara.

I.C. thanks the Ramón y Cajal program of the Ministerio de Economía Industria y Competitividad of Spain. I.C. and F.R.-G. also thankfully acknowledge financial support from the PGC2018-094644-B-C21 project of the Ministerio de Ciencia, Innovación y Universidades of Spain and the Red Española de Supercomputación, the CESGA Supercomputer Center (Finisterrae), and the Centro de Computación Científica of the UAM (CCC-UAM) for the generous allocation of computer time and for their continued technical support.

S.F. is grateful to Innovational Research Incentives Scheme Vidi 2017 with Project No. 016.Vidi.189.044, which is (partly) financed by the Dutch Research Council (NWO).

DATA AVAILABILITY

Raw data were generated at the Cartesius (SURFSara) and “Centro de Computación Científica” large scale facilities. Derived data supporting the findings of this study are available from the corresponding authors upon reasonable request.

REFERENCES

- ¹W. A. Velema, W. Szymanski, and B. L. Feringa, "Photopharmacology: Beyond proof of principle," *J. Am. Chem. Soc.* **136**, 2178–2191 (2014).
- ²J. Broichhagen, J. A. Frank, and D. Trauner, "A roadmap to success in photopharmacology," *Acc. Chem. Res.* **48**, 1947–1960 (2015).
- ³Z. L. Pianowski, "Recent implementations of molecular photoswitches into smart materials and biological systems," *Chem. Eur. J.* **25**, 5128–5144 (2019).
- ⁴A. Nair, P. Chauhan, B. Saha, and K. F. Kubatzky, "Conceptual evolution of cell signaling," *Int. J. Mol. Sci.* **20**, 3292 (2019).
- ⁵R. Weissleder and V. Ntziachristos, "Shedding light onto live molecular targets," *Nat. Med.* **9**, 123–128 (2003).
- ⁶W. Szymański, J. M. Beierle, H. A. V. Kistemaker, W. A. Velema, and B. L. Feringa, "Reversible photocontrol of biological systems by the incorporation of molecular photoswitches," *Chem. Rev.* **113**, 6114–6178 (2013).
- ⁷F. Hamon, F. Djedaini-Pilard, F. Barbot, and C. Len, "Azobenzenes—synthesis and carbohydrate applications," *Tetrahedron* **65**, 10105–10123 (2009).
- ⁸A. A. Beharry and G. A. Woolley, "Azobenzene photoswitches for biomolecules," *Chem. Soc. Rev.* **40**, 4422–4437 (2011).
- ⁹C. Renner and L. Moroder, "Azobenzene as conformational switch in model peptides," *ChemBioChem* **7**, 868–878 (2006).
- ¹⁰N. Harada, N. Koumura, and B. L. Feringa, "Chemistry of unique chiral olefins. 3. Synthesis and absolute stereochemistry of *trans*- and *cis*-1,1',2,2',3,3',4,4'-octahydro-3,3'-dimethyl-4,4'-biphenanthrylidene," *J. Am. Chem. Soc.* **119**, 7256–7264 (1997).
- ¹¹N. Koumura, R. W. J. Zijlstra, R. A. van Delden, N. Harada, and B. L. Feringa, "Light-driven monodirectional molecular rotor," *Nature* **401**, 152–155 (1999).
- ¹²A. S. Lubbe, Q. Liu, S. J. Smith, J. W. de Vries, J. C. M. Kistemaker, A. H. de Vries, I. Faustino, Z. Meng, W. Szymanski, A. Herrmann, and B. L. Feringa, "Photoswitching of DNA hybridization using a molecular motor," *J. Am. Chem. Soc.* **140**, 5069–5076 (2018).
- ¹³J. Finley, P.-Å. Malmqvist, B. O. Roos, and L. Serrano-Andrés, "The multi-state CASPT2 method," *Chem. Phys. Lett.* **288**, 299–306 (1998).
- ¹⁴B. O. Roos, P. R. Taylor, and P. E. M. Sigbahn, "A complete active space SCF method (CASSCF) using a density matrix formulated super-CI approach," *Chem. Phys.* **48**, 157–173 (1980).
- ¹⁵B. O. Roos, "The multiconfigurational (MC) self-consistent field (SCF) theory," in *Lecture Notes in Quantum Chemistry: European Summer School in Quantum Chemistry*, edited by B. O. Roos (Springer Berlin Heidelberg, Berlin, Heidelberg, 1992), pp. 177–254.
- ¹⁶B. O. Roos, "The complete active space self-consistent field method and its applications in electronic structure calculations," in *Advances in Chemical Physics* (John Wiley & Sons, Ltd, 2007), pp. 399–445.
- ¹⁷J. Gräfenstein and D. Cremer, "Can density functional theory describe multi-reference systems? Investigation of carbenes and organic biradicals," *Phys. Chem. Chem. Phys.* **2**, 2091–2103 (2000).
- ¹⁸Y. Shao, M. Head-Gordon, and A. I. Krylov, "The spin-flip approach within time-dependent density functional theory: Theory and applications to diradicals," *J. Chem. Phys.* **118**, 4807–4818 (2003).
- ¹⁹Y. A. Bernard, Y. Shao, and A. I. Krylov, "General formulation of spin-flip time-dependent density functional theory using non-collinear kernels: Theory, implementation, and benchmarks," *J. Chem. Phys.* **136**, 204103 (2012).
- ²⁰X. Zhang and J. M. Herbert, "Analytic derivative couplings for spin-flip configuration interaction singles and spin-flip time-dependent density functional theory," *J. Chem. Phys.* **141**, 064104 (2014).
- ²¹J. M. Herbert, X. Zhang, A. F. Morrison, and J. Liu, "Beyond time-dependent density functional theory using only single excitations: Methods for computational studies of excited states in complex systems," *Acc. Chem. Res.* **49**, 931–941 (2016).
- ²²N. Minezawa and M. S. Gordon, "Optimizing conical intersections by spin-flip density functional theory: Application to ethylene," *J. Phys. Chem. A* **113**, 12749–12753 (2009).
- ²³D. Casanova and A. I. Krylov, "Spin-flip methods in quantum chemistry," *Phys. Chem. Chem. Phys.* **22**, 4326–4342 (2020).
- ²⁴Y. Harabuchi, K. Keipert, F. Zahariev, T. Taketsugu, and M. S. Gordon, "Dynamics simulations with spin-flip time-dependent density functional theory: Photoisomerization and photocyclization mechanisms of *cis*-stilbene in $\pi\pi^*$ states," *J. Phys. Chem. A* **118**, 11987–11998 (2014).
- ²⁵Y. Li, F. Liu, B. Wang, Q. Su, W. Wang, and K. Morokuma, "Different conical intersections control nonadiabatic photochemistry of fluorene light-driven molecular rotary motor: A CASSCF and spin-flip DFT study," *J. Chem. Phys.* **145**, 244311 (2016).
- ²⁶N. Orms and A. I. Krylov, "Singlet-triplet energy gaps and the degree of diradical character in binuclear copper molecular magnets characterized by spin-flip density functional theory," *Phys. Chem. Chem. Phys.* **20**, 13127–13144 (2018).
- ²⁷E. Salazar and S. Faraji, "Theoretical study of cyclohexadiene/hexatriene photochemical interconversion using spin-flip time-dependent density functional theory," *Mol. Phys.* **118**, e1764120 (2020).
- ²⁸T. H. Dunning, "Gaussian basis sets for use in correlated molecular calculations. I. The atoms boron through neon and hydrogen," *J. Chem. Phys.* **90**, 1007–1023 (1989).
- ²⁹T. N. Truong and E. V. Stefanovich, "A new method for incorporating solvent effect into the classical, ab initio molecular orbital and density functional theory frameworks for arbitrary shape cavity," *Chem. Phys. Lett.* **240**, 253–260 (1995).
- ³⁰V. Barone and M. Cossi, "Quantum calculation of molecular energies and energy gradients in solution by a conductor solvent model," *J. Phys. Chem. A* **102**, 1995–2001 (1998).
- ³¹Y. Shao, Z. Gan, E. Epifanovsky, A. T. B. Gilbert, M. Wormit, J. Kussmann, A. W. Lange, A. Behn, J. Deng, X. Feng, D. Ghosh, M. Goldey, P. R. Horn, L. D. Jacobson, I. Kaliman, R. Z. Khaliullin, T. Kuš, A. Landau, J. Liu, E. I. Proynov, Y. M. Rhee, R. M. Richard, M. A. Rohrdanz, R. P. Steele, E. J. Sundstrom, H. L. III, P. M. Zimmerman, D. Zuev, B. Albrecht, E. Alguire, B. Austin, G. J. O. Beran, Y. A. Bernard, E. Berquist, K. Brandhorst, K. B. Bravaya, S. T. Brown, D. Casanova, C.-M. Chang, Y. Chen, S. H. Chien, K. D. Closser, D. L. Crittenden, M. Diedenhofen, R. A. DiStasio, Jr., H. Do, A. D. Dutoi, R. G. Edgar, S. Fatehi, L. Fusti-Molnar, A. Ghysels, A. Golubeva-Zadorozhnaya, J. Gomes, M. W. D. Hanson-Heine, P. H. P. Harbach, A. W. Hauser, E. G. Hohenstein, Z. C. Holden, T.-C. Jagau, H. Ji, B. Kaduk, K. Khistyayev, J. Kim, J. Kim, R. A. King, P. Klunzinger, D. Kosenkov, T. Kowalczyk, C. M. Krauter, K. U. Lao, A. D. Laurent, K. V. Lawler, S. V. Levchenko, C. Y. Lin, F. Liu, E. Livshits, R. C. Lochan, A. Luenser, P. Manohar, S. F. Manzer, S.-P. Mao, N. Mardirossian, A. V. Marenich, S. A. Maurer, N. J. Mayhall, E. Neuscamman, C. M. Oana, R. Olivares-Amaya, D. P. O'Neill, J. A. Parkhill, T. M. Perrine, R. Peverati, A. Prociuk, D. R. Rehn, E. Rosta, N. J. Russ, S. M. Sharada, S. Sharma, D. W. Small, A. Sodt, T. Stein, D. Stück, Y.-C. Su, A. J. W. Thom, T. Tsuchimochi, V. Vanovschi, L. Vogt, O. Vydrov, T. Wang, M. A. Watson, J. Wenzel, A. White, C. F. Williams, J. Yang, S. Yeganeh, S. R. Yost, Z.-Q. You, I. Y. Zhang, X. Zhang, Y. Zhao, B. R. Brooks, G. K. L. Chan, D. M. Chipman, C. J. Cramer, W. A. Goddard III, M. S. Gordon, W. J. Hehre, A. Klamt, H. F. Schaefer III, M. W. Schmidt, C. D. Sherrill, D. G. Truhlar, A. Warshel, X. Xu, A. Aspuru-Guzik, R. Baer, A. T. Bell, N. A. Besley, J.-D. Chai, A. Dreuw, B. D. Dunietz, T. R. Furlani, S. R. Gwaltney, C.-P. Hsu, Y. Jung, J. Kong, D. S. Lambrecht, W. Liang, C. Ochsenfeld, V. A. Rassolov, L. V. Slipchenko, J. E. Subotnik, T. Van Voorhis, J. M. Herbert, A. I. Krylov, P. M. W. Gill, and M. Head-Gordon, "Advances in molecular quantum chemistry contained in the Q-Chem 4 program package," *Mol. Phys.* **113**, 184–215 (2015).
- ³²A. D. Becke, "Density-functional thermochemistry. III. The role of exact exchange," *J. Chem. Phys.* **98**, 5648–5652 (1993).
- ³³T. Yanai, D. P. Tew, and N. C. Handy, "A new hybrid exchange–correlation functional using the coulomb-attenuating method (CAM-B3LYP)," *Chem. Phys. Lett.* **393**, 51–57 (2004).
- ³⁴J.-D. Chai and M. Head-Gordon, "Long-range corrected hybrid density functionals with damped atom–atom dispersion corrections," *Phys. Chem. Chem. Phys.* **10**, 6615–6620 (2008).
- ³⁵K. Andersson, P. A. Malmqvist, B. O. Roos, A. J. Sadlej, and K. Wolinski, "Second-order perturbation theory with a CASSCF reference function," *J. Phys. Chem.* **94**, 5483–5488 (1990).
- ³⁶G. Ghigo, B. O. Roos, and P.-Å. Malmqvist, "A modified definition of the zeroth-order Hamiltonian in multiconfigurational perturbation theory (CASPT2)," *Chem. Phys. Lett.* **396**, 142–149 (2004).

- ³⁷N. Forsberg and P.-Å. Malmqvist, "Multiconfiguration perturbation theory with imaginary level shift," *Chem. Phys. Lett.* **274**, 196–204 (1997).
- ³⁸F. Aquilante, R. Lindh, and T. Bondo Pedersen, "Unbiased auxiliary basis sets for accurate two-electron integral approximations," *J. Chem. Phys.* **127**, 114107 (2007).
- ³⁹B. G. Levine, J. D. Coe, and T. J. Martínez, "Optimizing conical intersections without derivative coupling vectors: Application to multistate multireference second-order perturbation theory (MS-CASPT2)," *J. Phys. Chem. B* **112**, 405–413 (2008).
- ⁴⁰M. J. Bearpark, M. A. Robb, and H. Bernhard Schlegel, "A direct method for the location of the lowest energy point on a potential surface crossing," *Chem. Phys. Lett.* **223**, 269–274 (1994).
- ⁴¹I. F. Galván, M. Vacher, A. Alavi, C. Angeli, F. Aquilante, J. Autschbach, J. J. Bao, S. I. Bokarev, N. A. Bogdanov, R. K. Carlson, L. F. Chibotaru, J. Creutzberg, N. Dattani, M. G. Delcey, S. S. Dong, A. Dreuw, L. Freitag, L. M. Frutos, L. Gagliardi, F. Gendron, A. Giussani, L. González, G. Grell, M. Guo, C. E. Hoyer, M. Johansson, S. Keller, S. Knecht, G. Kovačević, E. Källman, G. Li Manni, M. Lundberg, Y. Ma, S. Mai, J. P. Malhado, P. k. Malmqvist, P. Marquetand, S. A. Mewes, J. Norell, M. Olivucci, M. Oppel, Q. M. Phung, K. Pierloot, F. Plasser, M. Reiher, A. M. Sand, I. Schapiro, P. Sharma, C. J. Stein, L. K. Sørensen, D. G. Truhlar, M. Ugandi, L. Ungur, A. Valentini, S. Vancoillie, V. Veryazov, O. Weser, T. A. Wesolowski, P.-O. Widmark, S. Wouters, A. Zech, J. P. Zobel, and R. Lindh, "OpenMolcas: From source code to insight," *J. Chem. Theory Comput.* **15**, 5925–5964 (2019).
- ⁴²T. Shiozaki, "BAGEL: Brilliantly advanced general electronic-structure library," *Wiley Interdiscip. Rev.: Comput. Mol. Sci.* **8**, e1331 (2018).
- ⁴³S. A. Mewes, F. Plasser, A. Krylov, and A. Dreuw, "Benchmarking excited-state calculations using exciton properties," *J. Chem. Theory Comput.* **14**, 710–725 (2018).
- ⁴⁴A. Dreuw and M. Head-Gordon, "Single-reference ab initio methods for the calculation of excited states of large molecules," *Chem. Rev.* **105**, 4009–4037 (2005).
- ⁴⁵D. J. Tozer, R. D. Amos, N. C. Handy, B. O. Roos, and L. Serrano-ANDRES, "Does density functional theory contribute to the understanding of excited states of unsaturated organic compounds?," *Mol. Phys.* **97**, 859–868 (1999).
- ⁴⁶Y. Tawada, T. Tsuneda, S. Yanagisawa, T. Yanai, and K. Hirao, "A long-range-corrected time-dependent density functional theory," *J. Chem. Phys.* **120**, 8425–8433 (2004).
- ⁴⁷H. Iikura, T. Tsuneda, T. Yanai, and K. Hirao, "A long-range correction scheme for generalized-gradient-approximation exchange functionals," *J. Chem. Phys.* **115**, 3540–3544 (2001).
- ⁴⁸O. A. Vydrov and G. E. Scuseria, "Assessment of a long-range corrected hybrid functional," *J. Chem. Phys.* **125**, 234109 (2006).
- ⁴⁹I. V. Rostov, R. D. Amos, R. Kobayashi, G. Scalmani, and M. J. Frisch, "Studies of the ground and excited-state surfaces of the retinal chromophore using CAM-B3LYP," *J. Phys. Chem. B* **114**, 5547–5555 (2010).
- ⁵⁰I. V. Rostov, R. Kobayashi, and R. D. Amos, "Comparing long-range corrected functionals in the *cis-trans* isomerisation of the retinal chromophore," *Mol. Phys.* **110**, 2329–2336 (2012).
- ⁵¹Y. Li, W. Wang, and F. Liu, "Exploring the mechanism of a chiral *N*-alkyl imine-based light-driven molecular rotary motor at MS-CASPT2//CASSCF and MS-CASPT2//(TD) DFT levels," *Chem. - Eur. J.* **25**, 4194–4201 (2019).
- ⁵²M. Dierksen and S. Grimme, "The vibronic structure of electronic absorption spectra of large molecules: A time-dependent density functional study on the influence of 'exact' Hartree–Fock exchange," *J. Phys. Chem. A* **108**, 10225–10237 (2004).
- ⁵³D. R. Yarkony, "Diaboloical conical intersections," *Rev. Mod. Phys.* **68**, 985–1013 (1996).
- ⁵⁴T. J. Martinez, "Physical chemistry: Seaming is believing," *Nature* **467**, 412–413 (2010).
- ⁵⁵O. Tishchenko, J. Zheng, and D. G. Truhlar, "Multireference model chemistries for thermochemical kinetics," *J. Chem. Theory Comput.* **4**, 1208–1219 (2008).
- ⁵⁶A. D. Becke, "Density-functional exchange-energy approximation with correct asymptotic behavior," *Phys. Rev. A* **38**, 3098–3100 (1988).
- ⁵⁷C. Lee, W. Yang, and R. G. Parr, "Development of the Colle-Salvetti correlation-energy formula into a functional of the electron density," *Phys. Rev. B* **37**, 785–789 (1988).